11.4

MODEL SIMULATION AND REMOTE SENSING OF BORE AND SOLITARY WAVE MIXING PROCESSES

Steven E. Koch[1], Mariusz Pagowski[1,2], Bart Geerts[3], and Kristopher M. Bedka[4]

[1] *NOAA Earth System Research Laboratory (ESRL), Boulder, CO*
[2] *Cooperative Institute for Research in the Atmosphere (CIRA), Colorado State University, Ft. Collins, CO*
[3] *Department of Atmospheric Sciences, University of Wyoming, Laramie, WY*
[4] *Cooperative Institute for Meteorological Satellite Studies (CIMSS), University of Wisconsin – Madison*

1. INTRODUCTION

The International H2O Project (IHOP), which occurred over a six-week period in the southern Great Plains of the U.S. (Weckwerth et al. 2004), provided an unprecedented set of data to examine the detailed vertical structure and characteristics of density currents, bores, and solitons. Density currents are primarily horizontal mass flows driven by their greater density relative to their environment. In a stratified atmosphere, a density current may generate a hydraulic jump (a bore), associated with a sudden increase in the depth of the layer beneath the inversion (Simpson 1987; Crook 1988; Rottman and Simpson 1989). Under proper conditions, a bore may evolve into a family of solitary waves known as a "soliton" (Christie et al. 1979). A solitary wave consists of a single wave of elevation that, owing to a balance between nonlinearity and dispersion, propagates without change of form.

Bores and solitons were observed repeatedly by a large multitude of ground-based and airborne remote sensing systems. The primary objective of this study is to increase understanding of the mixing processes associated with these phenomena, and how this mixing affects the distribution of water vapor and aerosols. Two main types of instability are known for creating turbulent mixing in density currents: Kelvin-Helmholtz billows that roll up in the region of speed shear above the head of the current, and lobes and clefts formed by frictional effects on the lower part of the leading edge of the density current. The lobes lead to static instability through an overrunning of the denser fluid in the nose of the current over the lighter fluid. Billows appear to be the primary means by which air originating from above the inversion is mixed into a density current (Drogemeier and Wilhelmson 1985; Geerts et al. 2006).

When the depth of the density current (d_b) is greater than the depth of the stably stratified layer (h_0), the flow of the denser fluid within the density current is partially blocked and a bore is generated. The bore may separate from the density current and propagate ahead of it. Mixing processes in bores and solitons increase with the bore strength, defined as the ratio of the mean bore depth to the depth of the inversion layer (d_b/h_0). Laboratory experiments predict that when the bore strength lies in the range of $2 < d_b/h_0 < 4$, mixing commences behind the bore head on the downstream side of the first solitary wave, as well as at points further downstream where Kelvin-Helmholtz instability may arise (Rottman and Simpson 1989). However, very little is known about the nature of such mixing in the real atmosphere, nor how it may impact moisture and aerosol distributions.

The structure and dynamics of two bores generated during the early morning of 4 June 2002 over the Great Plains provide the basis of this study. This paper describes the instruments and analysis techniques used, the design of the nested high-resolution model experiments, and the results of the observational analysis and the model simulations, so as to develop a conceptual framework for understanding the nature of entrainment and turbulent mixing processes by the bores and solitons.

2. INSTRUMENT DESCRIPTION

All of the ground-based remote sensing systems were located at Homestead (HISS) in the Oklahoma Panhandle, with the exception of the S-POL radar, which was located 15 km to the west of Homestead. **S-POL** is an S-band dual-polarization Doppler radar, which also provided estimates of the low-level index of refraction within ~40 km from the radar following

Corresponding author address: *Steven E. Koch, NOAA/OAR/ESRL, R/GSD, 325 Broadway, Boulder, CO 80305-3328; e-mail <* Steven.Koch@noaa.gov*>*

the technique described in Fabry et al. (1997). The refractivity is a function of two terms: a dry density term and a moist term. As air temperature increases, the moist term increasingly dominates over the dry density term. High correlation between S-POL radar refractivity and that derived from nearby mesonet observations has been found (Weckwerth et al. 2005). A vertically pointing **FM-CW** radar detected fluctuations in the index of refraction over the lowest 2.5 km of the atmosphere with very high sensitivity to fluctuations as small as a few meters. The NCAR Multiple Antenna Profiler (**MAPR**) provided measurements of the horizontal and vertical wind components with 30-sec time resolution and 60-m height resolution to 4.0 km (Cohn et al. 2001). A Scanning Raman Lidar (**SRL**, Whiteman et al. 2006) and the Holographic Airborne Rotating Lidar Experiment (**HARLIE**, Schwemmer et al. 1998) were also used in this study. The SRL provided mixing ratio data with a temporal resolution of 2 min and a vertical resolution of ~30 m to 200 m. HARLIE is an aerosol backscatter lidar with an effective altitude resolution of ~50 m below 2-km altitude, degrading with height to ~250 m. Retrieved profiles of temperature and moisture were provided below cloud base every 10 min by the Atmospheric Emitted Radiance Interferometer (**AERI**) (Feltz et al. 2003; Knuteson et al. 2004) in the planetary boundary layer (PBL) below 2.5 km. with a vertical resolution of 50 m below 1 km, degrading to 250 m in the 2–3 km layers.

Special surface and sounding systems were also used in this study. Surface data with temporal sampling ranging from 1 min to 60 min were available from a collection of surface mesonetworks. The Integrated Sounding System (**ISS**, Cohn et al. 2001) provided detailed soundings at 3-h intervals. Lastly, the University of Wyoming King Air (UWKA) provided in situ measurements. The UWKA flew along a set of paths directed perpendicular to bore B.

3. NUMERICAL MODEL CONFIGURATION

Idealized numerical model simulations of density currents, bores, and solitons have added significantly to our understanding of these phenomena (e.g., Droegemeier and Wilhelmson 1985; Crook 1988; Haase and Smith 1989a, b; Jin et al. 1996), but the ability to simulate these phenomena accurately using a numerical weather prediction model initialized with actual observations is unproven. This study addressed this challenge by running a very high-resolution version of the MM5 model initialized with real data. The model was set up in a quadruple, one-way nested-grid configuration, at resolutions of 18, 6, 2, and 0.7-km grid mesh sizes, with the coarsest domain run initialized at 0000 UTC 4 June 2002. All but the finest grid used 32 vertically stretched sigma coordinate surfaces; the 0.7-km domain was run with 44 vertical levels, half of which were contained below the 1.5 km level to provide very high vertical resolution where it was most needed. The Burk and Thompson (1989) 2.5-level closure PBL scheme, the Blackadar surface scheme (Zhang and Anthes 1982), Reisner et al. (1998) mixed-phase microphysics, and the Mlawer et al. (1997) radiation scheme were employed. An experiment was also performed to examine the sensitivity of the results using the Eta model PBL scheme.

Dispersion of water vapor and aerosols is enhanced by the interaction of vertical shear and buoyancy. Under stable conditions, vertical mixing is delayed until the Richardson number becomes small enough to permit development of turbulent bursts. The Turbulent Kinetic Energy (TKE) provides the most direct measure of the turbulence intensity. At a grid-mesh size of 0.7 km, the MM5 model simulations approach the energy-containing eddy range of resolved turbulence. Although a true large-eddy simulation would require further decrease in the mesh size by a factor of ~10, an inverse cascade of energy toward larger scales from the resolvable scales may still occur in the finest mesh model run.

4. OBSERVATIONAL ANALYSES

The IHOP remote sensors sampled two bores during the early morning of 4 June 2002. Bore A developed from an outflow boundary that originated from convection in eastern New Mexico and crossed the Oklahoma Panhandle to the south of a synoptic quasi-stationary frontal boundary. The temperature contrast across this convergence boundary had already disappeared by 0430 UTC, two hours prior to its passage through the Homestead region. Bore B developed in association with postfrontal precipitation in west-central Kansas to the north of the east-west synoptic front. By the time that this bore reached the Homestead network at ~1030 UTC, there was no discernible cooling associated with its passage.

a. FM-CW, MAPR, SRL, and HARLIE observations

Passage of Bore A is apparent in the FM-CW reflectivity data (Fig. 1a) and the MAPR reflectivity and vertical motions (Figs. 1b, c). The bore had evolved into a soliton composed of waves with a horizontal wavelength of 15–16 km [estimated using time-to-space conversion and the bore propagation speed of 9.8 m s^{-1}]. The depth of the antecedent PBL (0.75 km) abruptly jumps to 1.3 km following the passage of the bore front at 0630 UTC, according to both FM-CW and MAPR. The MAPR signal-to-noise ratio data (Fig. 1b) imply an indirect influence of the bore to at least 3 km (increasing with the passage of the second and third waves at 0705 and 0735 UTC). The MAPR data reveal a quadrature (90^0) phase relation between the vertical motions and fluctuations in the height of the inversion. Updrafts of 1-1.5 m s^{-1} result in 0.6–0.8 km of lifting, which agrees quite well with the observed increase of the PBL depth.

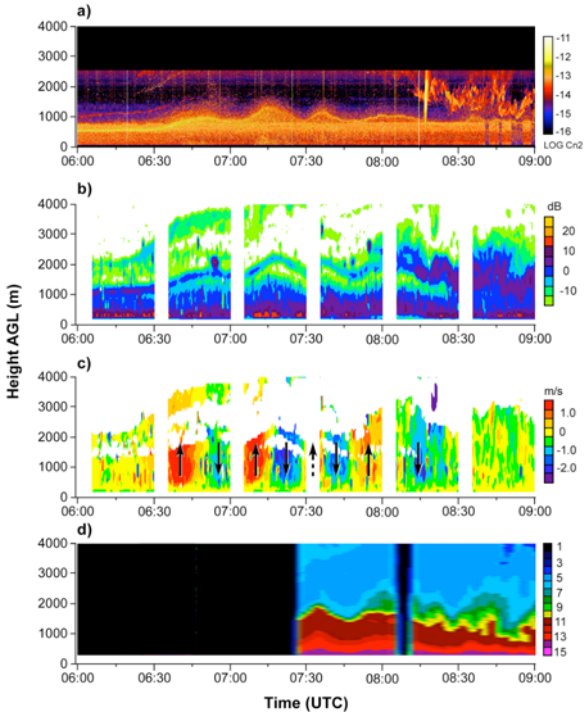

Fig. 1. a) FM-CW reflectivity (turbulence structure function units), b) MAPR signal-to-noise ratio (dB), c) MAPR vertical motions (m s^{-1}, red updrafts, blue downdrafts, and d) SLR mixing ratios (g kg^{-1}) for the period 0600–0900 UTC. Displays extend to 4.0 km AGL for purpose of making comparisons, though there is no FM-CW data above 2.5 km. Bore A passes sensors at 0630 UTC, resulting in sudden deepening of the stable boundary layer originally of 0.7 km depth to ~1.3 km depth, followed by three amplitude-ordered solitary waves.

HARLIE observations of aerosol backscatter returns are shown in Fig. 2a for the lowest 12 km of the atmosphere for a ±3.5-h period of time surrounding the passage of bore A and in Fig. 2b for the lowest 4 km for a ±1.0-h time segment centered on 0700 UTC. The larger-scale display illustrates the dramatic effects of mixing by the bore and subsequent waves, as aerosols are wafted through a 4-km deep layer following soliton passage; in addition, there is evidence of cloud development well above the bore. The zoomed-in display presents a clear picture of the bore and subsequent waves, and their influence on lifting and dispersing an elevated layer of high aerosol content originally present in the 1.5–2.0 km layer to above 4 km. This influence is likely the result of induced gravity waves in the overlying stable layer.

b. UW King Air observations

Bore B is readily apparent in measurements collected from the 1850 m flight leg of the UWKA aircraft as it flew through the crests of the solitary waves (Fig. 3). The aircraft intercepted the bore at 10:50:25 UTC just as it was passing over the Homestead facilities. Also apparent are two amplitude-ordered solitary waves with horizontal wavelengths of ~7 km. Changes experienced by the UWKA as it penetrated the bore consisted of 3 g kg^{-1} moistening, 3 C cooling, and 4 m s^{-1} increase in wind speed directed towards the rear of the bore. The sustained nature of the changes supports the interpretation of their source being a bore.

The small 0.15 hPa magnitude of the pressure jump suggests that the top of the bore is at 2.2 km, or 0.3 km above the flight level. The fact that the bore-relative winds are all negative means that the flow at the flight altitude is directed away from the bore head toward its rear, adding further support to the notion that the aircraft was flying near the top of the bore. This bore depth from the UWKA falls between the ~2.0 km estimate from FM-CW and the ~2.7 km obtained from MAPR. We suggest that a best estimate of the bore depth is 2.3±0.3 km.

a)

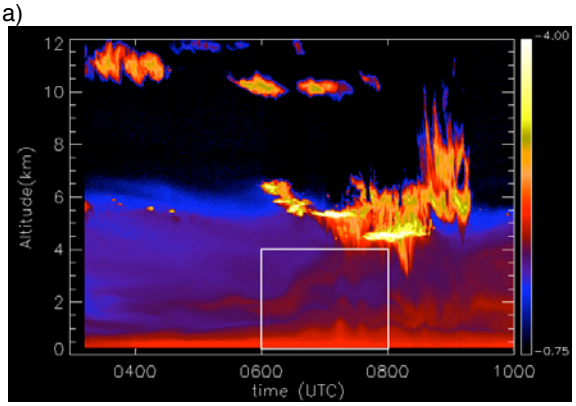

b)

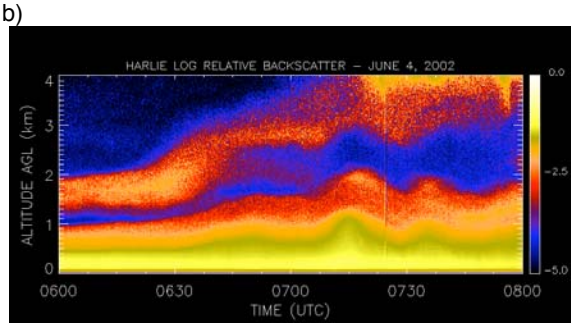

Fig. 2. HARLIE aerosol backscatter logarithmic signal displays of a) the lowest 12 km of the atmosphere from 0300–1000 UTC and b) the lowest 4 km of the atmosphere from 0600–0800 UTC (region depicted by white box in panel (a)). The stable boundary layer structure associated with the nocturnal inversion is disrupted by passage of bore A at 0630 UTC. Aerosols are subsequently wafted through a 4-km deep layer, as induced lifting above the bore associated with upward propagation of solitary wave energy forces vigorous mixing and possibly promotes cloud development at higher altitudes.

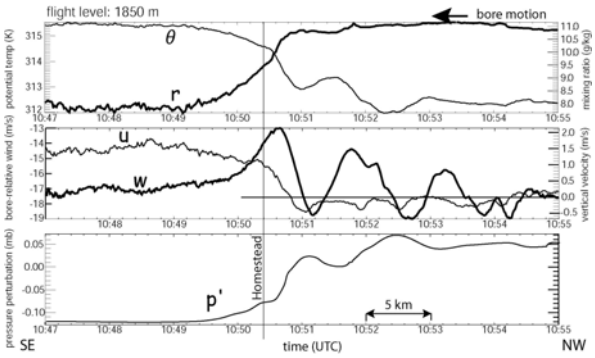

Fig. 3. Flight-level data from UW King Air flight taken from 1047–1055 UTC along a track perpendicular to bore B at 1850-m AGL. Top, middle, and bottom panels show, respectively, traces of: a) potential temperature (K, light line), mixing ratio (g kg^{-1}, thick line), b) bore-relative wind component assuming a bore velocity of 10.2 m s^{-1} from 330^{0} (m s^{-1}, light line, with negative values indicating flow from the front to the back of the bore) and vertical velocity (m s^{-1}, thick line), and c) pressure perturbation (hPa). Aircraft passed through the bore front at nearly the same time that the bore passed over Homestead (10:50:24). Note antiphase relationships between perturbations in potential temperature and pressure, and quadrature (quarter-wavelength) relationship between potential temperature and vertical velocity perturbations.

c. AERI observations of the bore thermodynamics

AERI time-height displays over the lowest 2 km of the atmosphere of refractivity (N), mixing ratio, and potential temperature, as well as "perturbation" fields (defined as a difference from the average at each level calculated over the entire time window), are presented in Fig. 4. These displays clearly reveal a bore signature consisting of an abrupt cooling of 1-3 C (strongest in the 500–1200 m layer) and rapid moistening throughout this layer. The lack of near-surface cooling is a feature characteristic of bores. A rapid increase of mixing ratio occurs with bore A, but less so with bore B, primarily because ample moisture had been infused into a 2 km deep layer by the earlier passage of bore A and the subsequent wavetrain (resulting in a doubling of the precipitable water from the surface to 2.5 km). The more gradual deepening of moisture above the PBL seen in the AERI data after ~0630 UTC corroborates the HARLIE observations indicative of aerosol wafting throughout the lowest 4 km.

Both bores produced pronounced *increases* of refractivity of ~6–8 units associated with sudden increases of mixing ratio of ~ 1–2 g kg^{-1} and slight cooling (except for the lowest 50 m). Note also the existence of a very shallow (<200-m deep) moist layer near the surface with no evidence of drying or refractivity decreases. Only 15 km to the west, near-surface refractivity change fields computed from S-POL and surface mesonet data during the times of bore passage both showed a band of pronounced rate of *decrease* in N (-7 to -10 units in 12 min) in association with the passage of bore A in the central Oklahoma Panhandle region. The primary cause for this sudden decrease in refractivity was a rapid drop in water vapor mixing ratio with negligible temperature change. However, this band virtually disappeared during its short progression to the Homestead facility.

These measurements made by AERI at the Homestead facility and the refractivity changes computed from S-POL and the mesonet data, together suggest that at earlier times, when the bore/soliton system was much stronger, downward mixing of warm, dry air from above the inversion within the solitary waves produced strong surface drying and decreases in refractivity. However, with the demise of the bore/soliton system near Homestead, this mixing apparently became much less vigorous. Consequently, during bore demise, lifting of air by the bore head only produced adiabatic cooling aloft with no surface drying, and distributed the very moist air near the surface upwards through the bore depth and beyond by the waves. This hypothesis lends itself to testing using the numerical model, as discussed next.

5. NUMERICAL MODEL RESULTS

None of the model simulations were able to produce anything like bore A. The reason for this failure is that the MM5 did not predict any deep convection over New Mexico or the western Oklahoma Panhandle from 0000 to 0900 UTC. On the other hand, the models successfully produced an impressive bore corresponding well in timing and location with observed bore B, because the models were able to better handle the quasi-stationary frontal system and the post-frontal precipitation. Furthermore, the highest-resolution (0.7 km) model was able to produce a soliton from this bore with characteristics nearly identical to those observed. These results indicate that the ability of NWP models to simulate observed bores and solitons is predicated on their ability to accurately simulate precipitation and to have sufficient resolution.

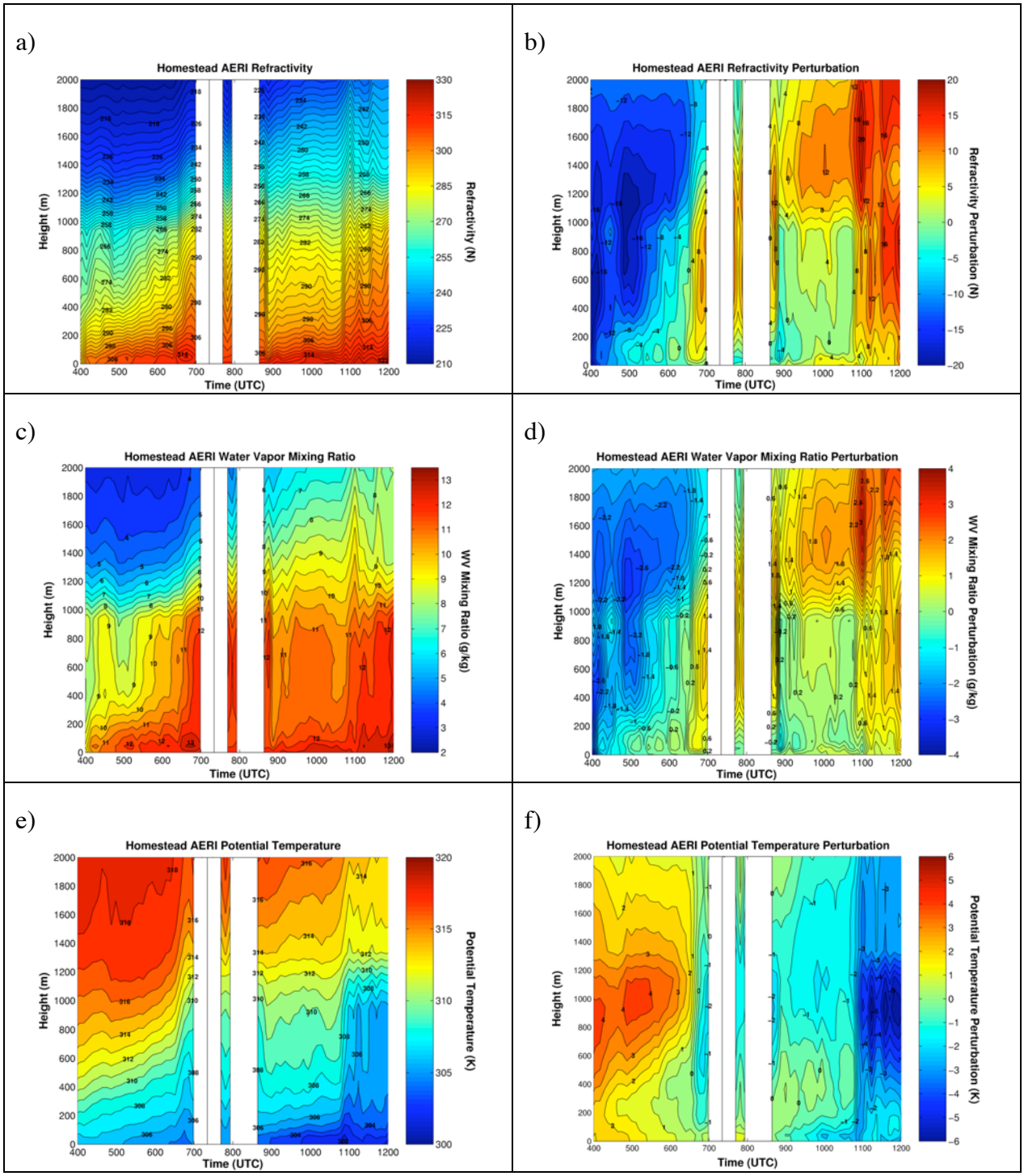

Fig. 4. AERI time-height displays from 0400–1200 UTC of a) refractivity (N units), b) perturbation refractivity (N units), c) mixing ratio (g kg^{-1}), d) perturbation mixing ratio (g kg^{-1}), e) potential temperature (K), and f) perturbation potential temperature (K). Passage of bores A and B occurs at 0625 and 1050 UTC, respectively.

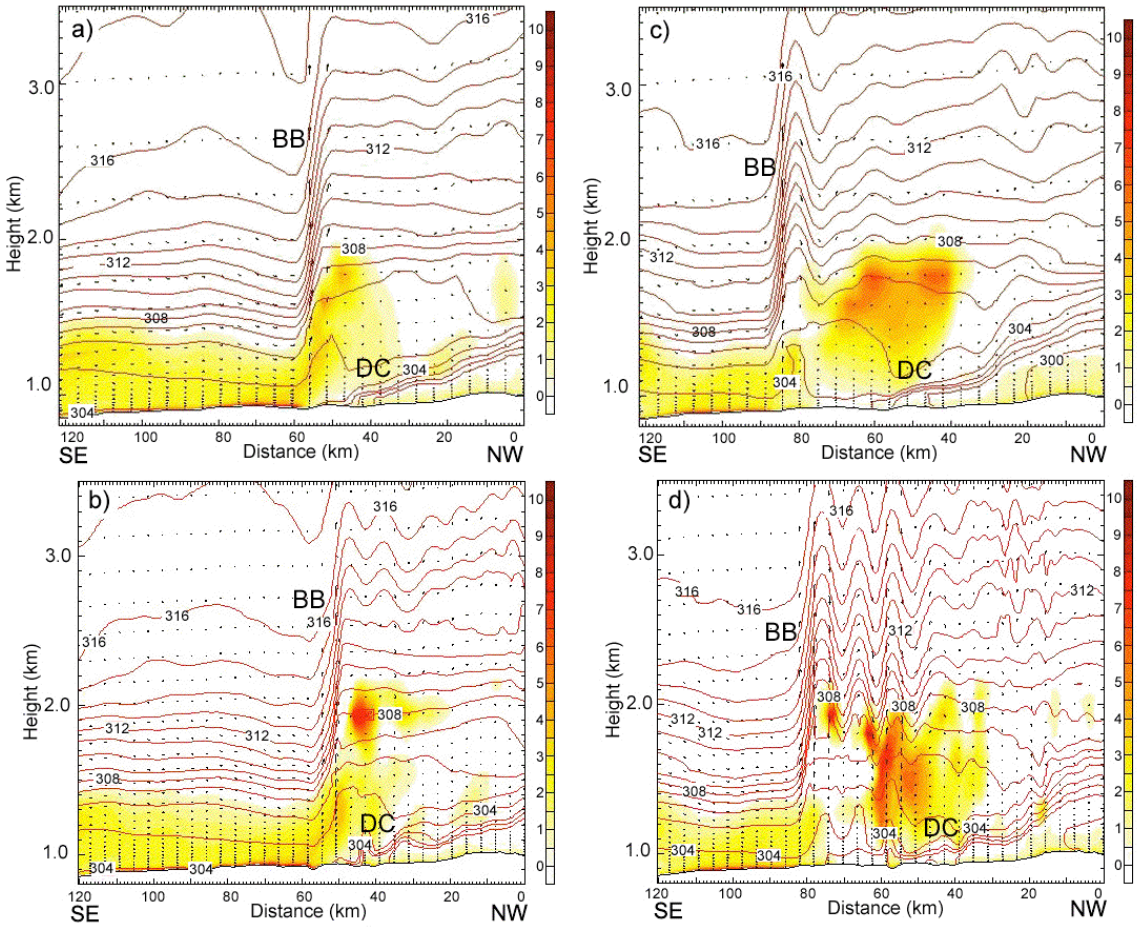

Fig. 5. Simulated potential temperature (1K isentropes), Turbulent Kinetic Energy (TKE, color-fill, J kg^{-1}), and two-dimensional vertical circulation fields at (a) 0800 from 2-km resolution model, (b) 0800 from 0.7-km resolution model, (c) 0900 from 2-km resolution model, and (d) 0900 UTC from 0.7-km resolution model. Cross section for both models is the same. Note that northwest (southeast) is to the right (left), in order to make comparison with the remote sensing systems more direct. Bore B (BB) propagates ahead of density current (DC) and evolves into an amplitude-order solitary wave system. Soliton never fully develops in 2-km simulation through the end of the model run. Bore speed is 9.5 m s^{-1} in 2-km simulation, 8.4 m s^{-1} in 0.7-km nested run.

a. Sensitivity to model grid resolution

The 0.7-km nested grid simulation and the 2-km resolution simulation both produced the density current and a phenomenon akin to observed bore B, and the high-resolution model also contained several solitary waves, as shown in a vertical cross section taken perpendicular to the bore (Fig. 5). The solitary waves display amplitude ordering and a horizontal wavelength of 9.3 km, which is comparable to 8.3 km averaged from the FM-CW, MAPR, and UWKA data. By contrast, the very weak waves in the 2-km simulation have an average wavelength of 11.6 km, which is smaller than six times the grid spacing, thus they are poorly resolved. The three waves composing the soliton at 0900 UTC in the fine-grid simulation increased to five waves during the subsequent hour, but did not multiply further afterwards. This behavior compares nicely with the observations.

The antecedent inversion surface is abruptly lifted during the progression of the bore to the southeast at a speed of 9.5 m s^{-1} in the fine grid simulation (compared to 10.2 m s^{-1} in the observations). The parent density current (the cold front) is visible 10 km to the northwest of the incipient bore at 0800 UTC, but this distance increases to nearly 30 km by 0900 UTC as the bore propagates ahead of the density current.

b. Turbulence and mixing in the simulations

The fine grid simulation places the strongest mixing (TKE) within the moist PBL ahead of the bore, directly behind the bore head, and underneath the solitary waves. The first of these three regions is easily understood to be the result of the shear stress

related to the strong along-bore flow associated with the low-level jet. This conjecture is supported by an independent calculation of this term (not shown). The other two regions are actually related to the same process, as revealed by detailed analysis of 15-min resolution plots. That analysis revealed the following repetitive process: (1) a local maximum in TKE originates in the first solitary wave trough right behind the bore head, (2) this local anomaly is advected rearward and downward by the vertical motions associated with this wave into the ridge region of the second wave, where it is subjected to vertical deformation, and (3) subsequently the anomaly undergoes a similar advection and stretching process as it progresses through the trough following the second wave and is mixed into the ridge of the third wave. As this feature makes its way rearward and downward, it becomes increasingly subjected to less static stability and the buoyancy generation of TKE is more important.

Further analysis of the fine grid simulation mixing processes (to be shown at the conference) revealed that mixing ratio was substantially reduced within each solitary wave trough due to entrainment of dry air above the inversion and subsidence. These dry intrusions penetrated to within 800 m of the surface. In addition, a drying effect also displaying a wavelike behavior was evident very near to the surface and under the wavetrain. Between these two regions, a layer of high mixing ratio existed. The bore-relative circulation revealed the existence of closed circulations beneath each of the waves within 500 m of the surface. Since no moisture could be advected from the rear towards the bore front, any dry air that was brought down to these very low levels by the wave-induced subsidence would be trapped near the surface. In fact, a time-height cross section of mixing ratio variations displayed very shallow drying at and following the bore passage. These processes were active prior to bore demise.

The turbulence sensor on the UWKA provided additional evidence supporting the model simulations of TKE and mixing processes (not shown). Strong turbulence was encountered at 240 m AGL behind the bore in association with the solitary waves. The TKE peaks displayed an average period of 111 sec, corresponding to a horizontal wavelength of 8.1 km given the ground speed of the aircraft minus the bore propagation speed. These data corroborate the model predictions showing strong TKE generation beneath each of the solitary waves.

6. CONCLUSIONS

Solitary wave trains associated with two bores were observed by a very large number of ground-based and airborne profiling systems during the International H2O Project (IHOP) and also numerically simulated with a multiply-nested numerical model down to a resolution of 0.7 km. This study marks the first successful attempt to use such a high-resolution numerical weather prediction (NWP) model initialized with real data to simulate an observed bore and solitary waves. The observations consisted of S-POL radar reflectivity data, three-dimensional winds from the NCAR Multiple Antenna Profiler (MAPR), boundary layer height fluctuations from a Frequency Modulation-Continuous Wave (FM-CW) radar, profiles of temperature and moisture retrieved by an Atmospheric Emitted Radiance Interferometer (AERI), and the NCAR Integrated Sounding System, all at the Homestead, Oklahoma observing site, plus surface mesonetwork data, and in situ measurements taken by the University of Wyoming King Air.

The model produced a feature that corresponded well in timing and location with the second of the two bores, but the first bore was not successfully simulated due to problems with forecasting convective precipitation correctly. Although both bores were in their dissipating stage when they passed over the Homestead observing site, the remote sensing systems all showed that the antecedent nocturnal inversion depth was nearly doubled by the passage of the bore. The observational and model data both showed that the bores wafted moist air up to the middle troposphere and weakened the capping inversion, thus reducing inhibition to deep convection development. Near-surface observations showed pronounced decreases in water vapor mixing ratio accompanied the passage of the bores during their active phase, but during bore collapse, moistening appeared in the lowest 0.5 km of the atmosphere.

The results indicate that low-level drying near the surface was due to vigorous downward turbulent mixing of air by the wave circulations. Turbulent kinetic energy was generated immediately behind the bore head, then advected rearward and downward by the solitary waves. During the dissipation stage, the lifting by the bore head produced adiabatic cooling aloft and distributed the very moist air near the surface upwards through the bore depth, but without any drying due to the absence of vigorous mixing.

This study shows that it is possible for NWP models to predict bores and solitons, and to be used as research tools, in combination with remote sensing systems, to understand the dynamics of these phenomena. However, the value of the model depends upon whether it can skillfully forecast observed precipitation patterns, given the sensitivity of the density current and bore occurrence to this factor. Other necessary ingredients for successful numerical simulation include the proper simulation of the waveguide, such as a frontal system acting as a horizontal delimiter, and the strength of the low-level

jet, which acts as an important mechanism for trapping vertical wave energy propagation.

7. ACKNOWLEDGMENTS

We wish to express our appreciation to the University Corporation for Atmospheric Research/Joint Office for Science Support (UCAR/JOSS) for creating the very useful composites of 1-min, 5-min, and 60-min surface mesonet datasets. Rita Roberts (NCAR) helped create the surface and radar composite analyses. Discussions with Crystal Pettet (NCAR) about the refractivity changes derived from AERI, S-POL, and the mesonet stations were helpful. Jeff Keeler and Tammy Weckwerth (NCAR) offered assistance in the interpretation of the FM-CW noise problems. Bill Brown (NCAR) provided information concerning the MAPR data, and Dave Whiteman and Belay Demoz (NASA) did likewise with the SRL data.

8. REFERENCES

Burk, S. D., and W. T. Thompson, 1989: A vertically nested regional numerical weather prediction model with second-order closure physics. *Mon. Wea. Rev.,* **117,** 2305–2324.

1989: Long nonlinear waves in the lower atmosphere. *J. Atmos. Sci.,* **46,** 1462–1491.

Christie, D.R., K.J. Muirhead and A.L. Hales, 1979: Intrusive density flows in the lower troposphere: A source of atmospheric solitons. *J. Geophys. Res.,* **84,** 4959–4970.

Cohn, S. A., W. O. J. Brown, C. L. Martin, M. E. Susedik, G. Maclean, and D. B. Parsons, 2001: Clear air boundary layer spaced antenna wind measurement with the Multiple Antenna Profiler (MAPR). *Ann. Geophys.*, **19,** 845–854.

Crook, N. A., 1988: Trapping of low-level internal gravity waves. *J. Atmos. Sci.,* **45,** 1533–1541.

Droegemeier, K. K., and R. B. Wilhelmson, 1985: Three-dimensional numerical modeling of convection produced by interacting thunderstorm outflows. Part I: Control simulation and low-level moisture variations. *J. Atmos. Sci*., **42,** 2381–2403.

Fabry, F., C. Frush, I. Zawadzki, and A. Kilambi, 1997: On the extraction of near-surface index of refraction using radar phase measurements from ground targets. *J. Atmos. Ocean. Tech*., **14,** 978–987.

Feltz, W. F., W. L. Smith, H. B. Howell, R. O. Knuteson, H. Woolf, and H. E. Revercomb, 2003: Near-continuous profiling of temperature, moisture, and atmospheric stability using the Atmospheric Emitted Radiance Interferometer (AERI). *J. Appl. Meteor.,* **42,** 584–597.

Geerts, B., R. Damiani, and S. Haimov, 2006: Fine-scale vertical structure of a cold front as revealed by airborne radar. *Mon. Wea. Rev.*, **134,** 251–272.

Haase, S. P., and R.K. Smith, 1989a: The numerical simulation of atmospheric gravity currents. Part I: Neutrally–stable environments. *Geophys. Astrophys. Fluid Dynamics*, **46,** 1–33.

_____, 1989b: The numerical simulation of atmospheric gravity currents. Part II: Environments with stable layers. *Geophys. Astrophys. Fluid Dynamics,* **46,** 35–51.

Jin, Y., S. E. Koch, Y.–L. Lin, F. M. Ralph, and C. Chen, 1996: Numerical simulations of an observed gravity current and gravity waves in an environment characterized by complex stratification and shear. *J. Atmos. Sci.*, **53,** 3570–3588.

Knuteson, R. O., F. A. Best, N. C. Ciganovich, R. G. Dedecker, T. P. Dirkx, S. Ellington, W. F. Feltz, R. K. Garcia, R. A. Herbsleb, H. B. Howell, H. E. Revercomb, W. L. Smith, and J. F. Short, 2004: Atmospheric Emitted Radiance Interferometer (AERI): Part I: Instrument Design, *J. Atmos. Oceanic Technol.*, **21,** 1763-1776.

Mlawer, E.J., S.J. Taubman, P.D. Brown, M.J. Iacono, and S.A. Clough, 1997: Radiative transfer for inhomogeneous atmospheres: RRTM, a validated correlated-k model for the longwave. *J. Geophys. Res.*, **102(D14)**, 16,663–16,682.

Reisner, J., R.J. Rasmussen, and R.T. Bruintjes, 1998: Explicit forecasting of supercooled liquid water in winter storms using the MM5 mesoscale model. *Quart. J. Roy. Meteor. Soc.,* **124,** 1071–1107.

Rottman, J.W., and J.E. Simpson, 1989: The formation of internal bores in the atmosphere: A laboratory model. *Quart. J. Roy. Meteor. Soc.***, 115,** 941–963.

Schwemmer, G., T. Wilkerson, and D. Guerra, 1998: Compact scanning lidar systems using holographic optics. *Proc. SPIE Vol. 3504, Optical Remote Sensing for Industry and Environmental Monitoring, SPIE,* 51–59.

Simpson, J. E., 1987: *Density Currents: in the Environment and the Laboratory*. Wiley & Sons, 244 pp.

Weckwerth, T. M., D. B. Parsons, S. E. Koch, J. A. Moore, M. A. LeMone, B. B. Demoz, C. Flamant, B. Geerts, J. Wang, and W. F. Feltz, 2004: An overview of the International H_2O Project (IHOP_2002) and some preliminary highlights. *Bull. Amer. Meteor. Soc.*, **85,** 253–277.

_____, C. R Pettet, F. Fabry, S. Park, M. A. LeMone, and J. W. Wilson, 2005: Radar refractivity retrieval: Validation and application to short-term forecasting. *J. Appl. Meteor.*, **44,** 285–300.

Whiteman, D. N., B. Demoz, P. Di Girolamo, J. Comer, I. Veselovskii, K. Evans, Z. Wang, M. Cadirola, K. Rush, G. Schwemmer, B. Gentry, S. H. Melfi, B. Mielke, D. Venable, and T. Van Hov, 2006: Raman lidar measurements during the International H2O Project. Part I: Instrumentation and analysis techniques. *J. Atmos. Ocean. Tech.*, **23,** 157–169.

Zhang, D.–L., and R. A. Anthes, 1982: A high–resolution model of the planetary boundary layer—sensitivity tests and comparisons with SESAME–79 data. *J. Appl. Meteor.*, **21,** 1594 – 1609.